Journal of Computational Physics 374 (2018) 1044–1060

Contents lists available at ScienceDirect

Journal of Computational Physics

www.elsevier.com/locate/jcp

A second order numerical scheme for the annealing of metal–intermetallic laminate composite: A ternary reaction system

Shenggao Zhou [a], Yu Wang [b], Xingye Yue [a], Cheng Wang [c,*]

[a] Department of Mathematics and Mathematical Center for Interdiscipline Research, Soochow University, 1 Shizi Street, Suzhou, 215006, Jiangsu, China
[b] School of Materials Science and Engineering, North University of China, Taiyuan, 030051, China
[c] Department of Mathematics, University of Massachusetts, Dartmouth, North Dartmouth, MA 02747-2300, United States of America

ARTICLE INFO

Article history:
Received 30 January 2018
Received in revised form 14 June 2018
Accepted 21 July 2018
Available online 2 August 2018

Keywords:
Second-order accuracy
Convergence analysis
Microstructure evolution
Growth kinetics
Ternary phase diagram
Interface morphology

ABSTRACT

Metal–Intermetallic Laminate (MIL) composites are laminate structures that are fabricated by optimizing unique benefits of constituent components to have attractive physical and mechanical features, such as high strength, stiffness, and toughness. The synthesis of MIL composites involves annealing reaction of multiple metallic elements at high temperatures. In this work, we propose, analyze, and implement a second-order semi-implicit scheme for the annealing of a ternary metallic reaction system. The robustness of such a numerical scheme is demonstrated by various numerical experiments, as well as the expected accuracy tests. At the theoretical level, we provide a detailed convergence analysis, which confirms the second-order accuracy in both the temporal and spatial discretization. Moreover, this numerical scheme is used to study the annealing process of the Al–Fe–Ni ternary system. The computation reproduces the formation of the Al-rich and Ni-rich layers in the annealing process. We present the computational results as diffusion paths in a ternary phase diagram, with a nice agreement with that of experimental data. We also study the growth kinetics of the two layers by calculating the rate constant and kinetic exponent of the reaction. The morphology of interfaces between different layers is thoroughly investigated as well. The computational results indicate that the numerical scheme is an effective, useful tool for predicting the microstructure evolution in the annealing process of a ternary reaction system.

1. Introduction

Metal–intermetallic-laminate (MIL) composites are laminate structures designed to optimize unique properties of intermetallics by incorporating layers of ductile reinforcement in efforts to increase toughness. The synthesis of MIL composites is processed at high temperatures by pressing alternatively stacked metallic foils of two different kinds in a composite synthesis

apparatus, as shown in Fig. 1. Reactive diffusion between the metallic foils does not stop until one kind of the foils are fully consumed to form intermetallic layers, while the other is remained as the residual metal layer. The physical and

* Corresponding author.
E-mail addresses: sgzhou@suda.edu.cn (S. Zhou), wangyudlut@gmail.com (Y. Wang), xyyue@suda.edu.cn (X. Yue), cwang1@umassd.edu (C. Wang).

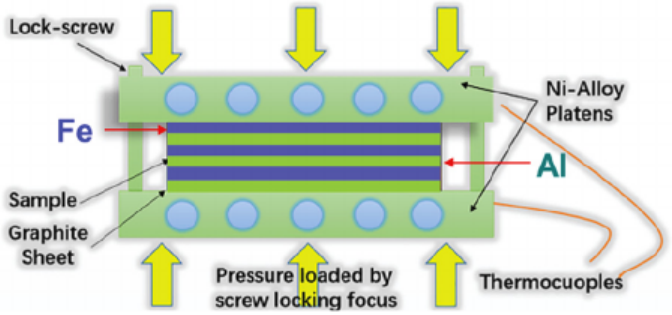

Fig. 1. Schematic view of MIL composite synthesis apparatus.

mechanical performance of the MIL composites can be significantly improved for specific applications by simply optimizing the width, stacking sequence, and compositions of the metallic foils [49].

The most extensively studied MIL composites are based on the Al–Ti system, in which the evolution of the microstructure of intermetallic phase, fracture behavior, and fatigue crack resistance have been systematically investigated in the literature [1,36,38]. The MIL composites based on Al–Ti system have shown great advantages in many mechanical properties, e.g., toughness [45]. To lower the production cost, it is desirable to replace the expensive Ti by other lower cost metallic material, such as Fe-based sheet metals. The MIL composites that are fabricated by pure iron and stainless steel have been systematically reported in the works [45,46,48,49]. The results have revealed that the microstructure, phase formation sequences, and growth kinetics of the intermetallic layer are highly related to the diffusional reaction between the stainless steel and Al foils, since the diffusion of the Fe, Al, Ni, and Cr elements in the system causes the chemical composites changing in the intermetallic layer of the iron-based MIL composites.

A theoretical model based on the diffusion equations of aluminum in pure iron has been proposed in the work [16]. Effective diffusion coefficients estimated from experimental data were used in the diffusion equations to compute aluminium composition profiles as a function of time, evaluate the coating growth rate, and calculate the morphology during aluminization. The assumption that diffusion coefficients are constant over entire concentration ranges may not apply effectively to the Al–Fe system, because the diffusion coefficients are more like functions of concentrations of different elements [25,33]. As a refinement to the model, diffusion equations with concentration-dependent diffusion coefficients were developed to analyze the kinetics of aluminization process [32]. Later, such equations have been successfully applied to qualitatively predict the growth kinetics and Al concentration during high-temperature annealing reactions [49]. However, the calculated concentration profiles exhibited discrepancies from the measured profile at the Al-rich intermetallic layer, in which the Al_2Fe intermetallic phase coexists with the Al_8Cr_5 intermetallic phase when Cr presents in the system. To consider the impact of a third metal element on the aluminization, a cross-diffusion system have been derived to describe the annealing reactions in a ternary system [33].

In this work, we consider the diffusion of two solute elements in an Fe-based system with the equations [32,49]

$$\begin{cases} u_t = -\nabla \cdot J_u, \\ v_t = -\nabla \cdot J_v, \end{cases}$$

where J_u and J_v are the fluxes of two components in the system:

$$J_u = -\ D^{uu}(u,v)\nabla u(x,y,z,t) + D^{uv}(u,v)\nabla v(x,y,z,t)\ ,$$
$$J_v = -\ D^{vu}(u,v)\nabla u(x,y,z,t) + D^{vv}(u,v)\nabla v(x,y,z,t)\ .$$

Taking an Al–Ni–Fe system as an example, u and v are the concentrations of Al and Ni, respectively, and $D^{uu}(u,v)$, $D^{uv}(u,v)$, $D^{vu}(u,v)$, and $D^{vv}(u,v)$ are given concentration-dependent diffusion coefficients in an Fe-based reaction system.

Altogether, we have the following diffusion equations

$$\begin{cases} u_t = \nabla \cdot \left[D^{uu}(u, v)\nabla u(x, y, z, t) + D^{uv}(u, v)\nabla v(x, y, z, t) \right], & (x, y, z) \in \Omega, \\ v_t = \nabla \cdot \left[D^{vu}(u, v)\nabla u(x, y, z, t) + D^{vv}(u, v)\nabla v(x, y, z, t) \right], & (x, y, z) \in \Omega, \end{cases} \tag{1.1}$$

where $\Omega = [-L_x, L_x] \times [-L_y, L_y] \times [-L_z, L_z]$. The initial and boundary conditions are given by

$$u(x, y, z, 0) = u_0(x, y, z), \ v(x, y, z, 0) = v_0(x, y, z) \ \text{ in } \Omega, \tag{1.2}$$

$$J_u \cdot \mathbf{n} = 0, \ J_v \cdot \mathbf{n} = 0 \ \text{ on } \partial\Omega \times (0, T]. \tag{1.3}$$

Here zero-flux boundary conditions are imposed to describe that there is no further supply of the material on the boundary.

The initial-boundary value problem of (1.1), (1.2), and (1.4) describes the evolution of each metal element under the influence of both self and cross diffusion. The nonlinear dependence of diffusion coefficients on concentrations poses a challenging task in the analysis of cross diffusion. Mathematical analysis on similar diffusion systems with cross diffusion has been well established in the literature, especially in the area of population dynamics [2–5,9,12,28–31,34,42]. For instance, the local and global-in-time existence of bounded weak solutions to cross-diffusion systems has been systematically studied with entropy methods [12,28,29]. In this work, we focus on numerically solutions of the problem to understand the evolution of the microstructure, growth kinetics, and interfacial morphology of intermetallic layers in a ternary reaction system.

Many numerical methods have been developed to solve a cross-diffusion system. Finite volume schemes that can preserve certain physical properties of the analytical solution have gained much attention. A convergent finite volume scheme of second order was developed to numerically solve a cross-diffusion model in population dynamics [5]. The scheme was applied to simulate pattern formation in cross-diffusion systems [39]. A finite volume scheme that preserves entropy structure in discrete level was proposed to solve a Keller–Segel model with cross diffusion [11]. Recently, an unconditionally stable, linear finite volume method was proposed for general nonlinear cross-diffusion systems. Error estimates in L^2 norm were also established rigorously [35]. Other numerical methods, based on finite element [6] and finite difference approximations [10], were also developed for cross diffusion models.

In this work, we propose a linear, semi-implicit finite difference scheme for a nonlinear cross-diffusion system with concentration-dependent diffusion coefficients. Based on the technique of linearized stability analysis [23,40,43], a theoretical justification of the convergence analysis is presented. Such analysis confirms that the numerical scheme is both second-order accurate in the spatial and temporal discretizations. The proposed numerical scheme is further applied to characterize the annealing process of a ternary reaction system that consists of Al, Ni, and Fe. Numerical simulations capture the formation of an Al-rich layer and Ni-rich layer. The growth kinetics of such two layers is analyzed by finding the rate constant and kinetic exponent of the reaction. The diffusion paths displayed in a ternary phase diagram show that simulation results are in a reasonable agreement with experimental data. In addition, we investigate the evolution of the morphology of interfaces between layers, starting from a randomly perturbed initial cross-section interface between Al layer and stainless steel layer. Overall, comparison between our simulation results and experimental data shows that our numerical scheme is an effective and useful method in predicting the microstructure of the annealing process of a ternary reaction system.

We use standard notation for Sobolev spaces [22]. Unless otherwise stated, we make the following assumptions throughout the rest of the paper:

(A1) The domain $\Omega \subset \mathbb{R}^3$ is a bounded and open cuboid with a boundary $\Gamma = \partial\Omega$.
(A2) The exact solution $U(x, t)$ and $V(x, t)$ has the regularity $C^3(0, T; C^0) \cap C^2(0, T; C^2) \cap L^\infty(0, T; C^4)$ for some positive T.
(A3) The diffusion coefficients $D^{uu}(u, v)$ and $D^{vv}(u, v)$ are given positive functions. Also, for any bounded u and v, we have $\|\partial_\gamma D^{\alpha\beta}(u, v)\|_{L^\infty} \le \bar{C}$ for $\alpha, \beta, \gamma = u$ or v, where $\bar{C}$ is a positive constant. Moreover,

$$D^{uu}(u, v) - \frac{|D^{uv}(u, v) + D^{vu}(u, v)|}{2} \ge d^u \text{ and } D^{vv}(u, v) - \frac{|D^{uv}(u, v) + D^{vu}(u, v)|}{2} \ge d^v$$

hold for any bounded u and v, where d^u and d^v are two positive constants.

Remark 1.1. We assume that the self-diffusion coefficients are greater than the average of the other two cross-diffusion

coefficients by lower bounds d and d. This assumption is justified by the fact that the diffusion coefficient of a species in its own environment is larger than that of the environment of other species [25]. From the activation energy point of view, the self diffusion of atoms only involves overcoming the lattice bondings between the same species of atoms in the crystal structure. In addition, the activation energy of self diffusion can be lowered by atoms substitution due to the imperfection in the structure. In contrast, cross diffusion in heterogeneous crystal structure needs to break the lattice bondings between atoms of different species, leading to higher activation energies.

This paper is organized as follows. In Section 2 we propose a second order finite difference scheme, and provide a detailed convergence analysis. In Section 3 we present the numerical convergence test and a few numerical simulation results, as well as the comparison with experimental data. Some concluding remarks are made in Section 4. Also, the error estimate in the first time step is given in Appendix A.1.

2. Numerical scheme and convergence analysis

2.1. Finite difference scheme

$$(x_i, y_j, z_k) = (-L_x + ih, -L_y + jh, -L_z + kh), \quad i = 0, \dots, N_x;\ j = 0, \dots, N_y;\ k = 0, \dots, N_z.$$

We denote by $t_n = n\Delta t$ $(n = 0, 1, \dots, N_t)$. For any function $f = f(x, y, z, t) : \Omega \times [0, T] \to \mathbb{R}$, we denote by $f^n_{i,j,k}$ approximations of $f(x_i, y_j, z_k, t_n)$, and define $f^n_{i\pm1/2,j,k} = \frac{1}{2} f^n_{i,j,k} + \frac{1}{2} f^n_{i\pm1,j,k}$ for $i = 1, \dots, N_x - 1$, $j = 1, \dots, N_y - 1$, $k = 1, \dots, N_z - 1$, and $n = 1, \dots, N_t$. Subsequently, the following discrete operators are introduced:

$$\delta_x f_{i+1/2,j,k} := \frac{f_{i+1,j,k} - f_{i,j,k}}{h}, \quad \delta_x f_{i-1/2,j,k} := \frac{f_{i,j,k} - f_{i-1,j,k}}{h}.$$

We notice that the first order difference approximation is evaluated at the staggered mesh points, instead of the regular vertex points. Similarly, δ_y and δ_z can be analogously defined. The discrete gradient operator becomes

$$\nabla_h f_{i,j,k} := (\delta_x f_{i+1/2,j,k}, \delta_y f_{i,j+1/2,k}, \delta_z f_{i,j,k+1/2}),$$

and the discrete Laplacian operator is given by

$$\nabla_h \cdot \nabla_h f_{i,j,k} := \frac{\delta_x f_{i+1/2,j,k} - \delta_x f_{i-1/2,j,k}}{h} + \frac{\delta_y f_{i,j+1/2,k} - \delta_y f_{i,j-1/2,k}}{h} + \frac{\delta_z f_{i,j,k+1/2} - \delta_z f_{i,j,k-1/2}}{h}.$$

Also, the following discrete operators (in time) are introduced:

$$E^1 f^n := \frac{3}{2} f^n - \frac{1}{2} f^{n-1}, \quad E^2 f^n := \frac{3}{4} f^{n+1} + \frac{1}{4} f^{n-1}.$$

The averaging operator E^1 keeps the linear nature of the proposed numerical scheme, while the averaging operator E^2 will greatly facilitate the convergence analysis, since more weights has been placed at the implicit level f^{n+1}, as will be demonstrated in later sections.

To solve the problem (1.1) to (1.4), we propose a fully discrete scheme

$$\begin{cases} \dfrac{u^{n+1}_{i,j,k} - u^n_{i,j,k}}{\Delta t} = \nabla_h \cdot \left[D^{uu}(E^1 u^n_{i,j,k}, E^1 v^n_{i,j,k}) \nabla_h E^2 u^n_{i,j,k} \right] \\ \qquad\qquad + \nabla_h \cdot \left[D^{uv}(E^1 u^n_{i,j,k}, E^1 v^n_{i,j,k}) \nabla_h E^2 v^n_{i,j,k} \right], \\ \dfrac{v^{n+1}_{i,j,k} - v^n_{i,j,k}}{\Delta t} = \nabla_h \cdot \left[D^{vu}(E^1 u^n_{i,j,k}, E^1 v^n_{i,j,k}) \nabla_h E^2 u^n_{i,j,k} \right] \\ \qquad\qquad + \nabla_h \cdot \left[D^{vv}(E^1 u^n_{i,j,k}, E^1 v^n_{i,j,k}) \nabla_h E^2 v^n_{i,j,k} \right]. \end{cases} \tag{2.1}$$

Here

$$\left[D^{uu}_{i+1/2,j,k} \delta_x E^2 u^n_{i+1/2,j,k} - D^{uu}_{i-1/2,j,k} \delta_x E^2 u^n_{i-1/2,j,k} \right]$$

$$\nabla_h \cdot \left[D \quad (E\ u_{i,j,k}, E\ v_{i,j,k}) \nabla_h E\ u_{i,j,k} \right] = \quad \frac{}{h}$$
$$+ \frac{D^{uu}_{i,j+1/2,k} \delta_y E^2 u^n_{i,j+1/2,k} - D^{uu}_{i,j-1/2,k} \delta_y E^2 u^n_{i,j-1/2,k}}{h}$$
$$+ \frac{D^{uu}_{i,j,k+1/2} \delta_z E^2 u^n_{i,j,k+1/2} - D^{uu}_{i,j,k-1/2} \delta_z E^2 u^n_{i,j,k-1/2}}{h},$$

where

$$D^{uu}_{i\pm1/2,j,k} = D^{uu}\left(\frac{1}{2}E^1 u^n_{i,j,k} + \frac{1}{2}E^1 u^n_{i\pm1,j,k}, \frac{1}{2}E^1 v^n_{i,j,k} + \frac{1}{2}E^1 v^n_{i\pm1,j,k}\right),$$
$$D^{uu}_{i,j\pm1/2,k} = D^{uu}\left(\frac{1}{2}E^1 u^n_{i,j,k} + \frac{1}{2}E^1 u^n_{i,j\pm1,k}, \frac{1}{2}E^1 v^n_{i,j,k} + \frac{1}{2}E^1 v^n_{i,j\pm1,k}\right),$$
$$D^{uu}_{i,j,k\pm1/2} = D^{uu}\left(\frac{1}{2}E^1 u^n_{i,j,k} + \frac{1}{2}E^1 u^n_{i,j,k\pm1}, \frac{1}{2}E^1 v^n_{i,j,k} + \frac{1}{2}E^1 v^n_{i,j,k\pm1}\right).$$

The other three terms on the right hand side of (2.1) are analogously defined. We notice that (2.1) is a three-step, semi-implicit linear scheme, with an implicit treatment for $\nabla_h E^2 u^n$, $\nabla_h E^2 v^n$, respectively.

Since three time steps are involved in (2.1), we compute the first time step by the following two-level semi-implicit scheme

$$\left\{ \frac{u^1_{i,j,k} - u^0_{i,j,k}}{} = \nabla_h \cdot \left[D^{uu}(u^0_{\cdot,\cdot,\cdot}, v^0_{\cdot,\cdot,\cdot}) \nabla_h u^1_{\cdot,\cdot,\cdot} \right] + \nabla_h \cdot \left[D^{uv}(u^0_{\cdot,\cdot,\cdot}, v^0_{\cdot,\cdot,\cdot}) \nabla_h v^1_{\cdot,\cdot,\cdot} \right], \right.$$

We now discuss the discretization of the boundary conditions (1.4). For simplicity of presentation, we only look at the boundary section where $x = -L_x$. To implement (2.1), a layer of ghost points, with indices $(-1, j, k)$, has to be introduced. Such ghost points are eliminated by the following equations obtained from central difference approximations of boundary conditions:

$$\frac{u_{-1,j,k} - u_{1,j,k}}{2h} = 0 \ \text{ and } \ \frac{v_{-1,j,k} - v_{1,j,k}}{2h} = 0.$$

Analogously, Neumann boundary conditions on the other boundary sections can be imposed in a similar way.

Remark 2.1. In this article, we use the vertex-centered finite difference grid. i.e., the physical variables (u, v) are evaluated at the regular grid points (x_i, y_j, z_k). This approach seems more standard to a beginner in numerical analysis. On the other hand, since Neumann boundary conditions have been imposed for the PDE system, a cell-centered finite difference approach, i.e., the approach with the physical variables evaluated at cell-centered mesh points $(x_{i+1/2}, y_{j+1/2}, z_{k+1/2})$, would enjoy more advantages than a vertex-centered one. For instance, a careful Taylor expansion reveals a smaller truncation error for the cell-centered one than the vertex-centered one, although both truncation errors correspond to the same accuracy order. And also, the summation formula for the cell-centered one takes a simpler form than that of the vertex-centered one, in the process of discrete energy estimate.

The cell-centered finite difference approximation has been successfully applied to the Cahn–Hilliard–Hele–Shaw equation in the existing literature [13,14,50], with homogeneous Neumann boundary condition. Its application to various gradient flows, such as phase field crystal, epitaxial thin film growth and functionalized Cahn–Hilliard models, has also been extensively studied in recent years [7,8,15,19–21,24,26,37,41,44,51], etc. All the numerical analyses presented in this article could be naturally extended to the finite difference scheme with cell-centered approximation, and the technical details are left to interested readers.

The main theoretical result of this article is given by the following theorem.

Theorem 2.1. *For any final time $T^* > 0$, assume that the exact solution (U, V) to equations (1.1)–(1.2) satisfies the assumption (A2). Denote $u_{\Delta t,h}$, $v_{\Delta t,h}$ as the fully discrete numerical solution given by the scheme (2.1). There exist two positive constants C_h and C_r such that, when $h \le C_h$ and $\Delta t \le C_r h$, the following convergence result is valid:*

$$\| u_{\Delta t,h} - U \|^2_{\infty,(0,T^*)} + \| v_{\Delta t,h} - V \|^2_{\infty,(0,T^*)} \le C_r (\Delta t^2 + h^2) \qquad (2.2)$$

$$\|u^{\Delta t,h} - U\|_{\ell^\infty(0,T^*;\ell^2)} + \|v^{\Delta t,h} - V\|_{\ell^\infty(0,T^*;\ell^2)} \le C\left(\Delta t^2 + h^2\right). \tag{2.3}$$

Note that the convergence constant in (2.3) also depends on the exact solution as well as T^*.

Although there have been extensive numerical simulation works for the cross-diffusion system [5,6,10,11,35,39], our proposed scheme (2.1) is the first numerical algorithm to theoretically justify the second order convergence, both in time and space.

2.2. Convergence analysis

To facilitate the numerical analysis, we define the discrete inner products for grid functions. For any pair of grid functions ϕ and ψ, which are defined at grid points (x_i, y_j, z_k), the discrete ℓ^2-inner product is given by

$$\langle \phi, \psi \rangle_{x,j,k} = h\left(\frac{1}{2}\phi_{0,j,k}\psi_{0,j,k} + \sum_{i=1}^{N_x-1}\phi_{i,j,k}\psi_{i,j,k} + \frac{1}{2}\phi_{N_x,j,k}\psi_{N_x,j,k}\right),$$

$$\langle \phi, \psi \rangle_{xy,k} = h\left(\frac{1}{2}\langle \phi, \psi \rangle_{x,0,k} + \sum_{j=1}^{N_y-1}\langle \phi, \psi \rangle_{x,j,k} + \frac{1}{2}\langle \phi, \psi \rangle_{x,N_y,k}\right),$$

$$\langle \phi, \psi \rangle = h\left(\frac{1}{2}\langle \phi, \psi \rangle_{xy,0} + \sum_{k=1}^{N_z-1}\langle \phi, \psi \rangle_{xy,k} + \frac{1}{2}\langle \phi, \psi \rangle_{xy,N_z}\right).$$

The associated discrete ℓ^2-norm is given by $\|\phi\|_2 := \sqrt{\langle \phi, \phi \rangle}$. For any pair of grid functions η^x and μ^x, which are defined at grid points $(x_{i+1/2}, y_j, z_k)$, the discrete ℓ^2-inner product along x direction is given by

Analogously, $(\cdot,\cdot)_y$ and $(\cdot,\cdot)_z$ can be defined. For any pair of grid functions ϕ and ψ on points (x_i, y_j, z_k), the discrete inner product of gradients is given by

$$(\nabla_h\phi, \nabla_h\psi) := (\delta_x\phi, \delta_x\psi)_x + (\delta_y\phi, \delta_y\psi)_y + (\delta_z\phi, \delta_z\psi)_z.$$

The associated discrete norm is given by $\|\nabla_h\phi\|_2 := \sqrt{(\nabla_h\phi, \nabla_h\phi)}$. A careful application of Taylor expansion reveals that, these discrete ℓ^2-inner product and ℓ^2-norm correspond to $O(h^2)$ approximations to the continuous version of the L^2-inner product and L^2 norm. In addition, we define discrete ℓ^∞-norm

$$\|\phi\|_\infty := \max_{i,j,k}|\phi_{i,j,k}|.$$

For the discrete inner products, we have the following two lemmas; see the related references [14,40], etc.

Lemma 2.1. *If grid functions ϕ and ψ satisfy the homogeneous Neumann boundary condition (1.4) on $\partial\Omega$, we have*

$$\langle \nabla_h \cdot \nabla_h\phi, \psi \rangle = -(\nabla_h\phi, \nabla_h\psi).$$

Lemma 2.2. *For any grid functions ϕ in 3D, we have the following inverse inequality*

$$\|\phi\|_\infty \le \frac{C^I}{h^{\frac{3}{2}}}\|\phi\|_2,$$

where C^I is a positive coefficient independent of grid size h.

The proof of Lemma 2.2 comes from a straightforward calculation, corresponding to the finite element version of inverse inequalities; we cite this result from an existing work [40], as Lemma 4.5.

Now we proceed into the proof of Theorem 2.1.

Proof. Given the exact solution $U(x,t)$ and $V(x,t)$ of the problem (1.1), (1.2), and (1.4), it follows from the Taylor expansion at $(x_i, y_j, z_k, t^{n+1/2})$ that

$$\begin{cases} \dfrac{U^{n+1}_{i,j,k} - U^n_{i,j,k}}{\Delta t} = \nabla_h \cdot \Big(D^{uu}(E^1 U^n_{i,j,k}, E^1 V^n_{i,j,k}) \nabla_h E^2 U^n_{i,j,k} \\ \qquad\qquad + D^{uv}(E^1 U^n_{i,j,k}, E^1 V^n_{i,j,k}) \nabla_h E^2 V^n_{i,j,k} \Big) + R^{U,n+1/2}_{i,j,k}, \\ \dfrac{V^{n+1}_{i,j,k} - V^n_{i,j,k}}{\Delta t} = \nabla_h \cdot \Big(D^{vu}(E^1 U^n_{i,j,k}, E^1 V^n_{i,j,k}) \nabla_h E^2 U^n_{i,j,k} \\ \qquad\qquad + D^{vv}(E^1 U^n_{i,j,k}, E^1 V^n_{i,j,k}) \nabla_h E^2 V^n_{i,j,k} \Big) + R^{V,n+1/2}_{i,j,k}, \end{cases} \tag{2.4}$$

where the truncation errors are given by

$$\begin{aligned} R^{U,n+1/2}_{i,j,k} &= \Delta t^2 f^{U,n+1/2}_{i,j,k} + h^2 g^{U,n+1/2}_{i,j,k}, \\ R^{V,n+1/2}_{i,j,k} &= \Delta t^2 f^{V,n+1/2}_{i,j,k} + h^2 g^{V,n+1/2}_{i,j,k}, \end{aligned} \tag{2.5}$$

with $f^{U,n+1/2}_{i,j,k}$, $f^{V,n+1/2}_{i,j,k}$, $g^{U,n+1/2}_{i,j,k}$, and $g^{V,n+1/2}_{i,j,k}$ associated with certain high order derivatives of exact solutions U and V.

The error functions are defined over the grid points:

$$\begin{cases} \dfrac{\tilde{u}^{n+1}_{i,j,k} - \tilde{u}^n_{i,j,k}}{\Delta t} = \nabla_h \cdot \Big(D^{uu}(E^1 u^n_{i,j,k}, E^1 v^n_{i,j,k}) \nabla_h E^2 \tilde{u}^n_{i,j,k} \\ \qquad + \Big(D^{uu}_1 E^1 \tilde{u}^n_{i,j,k} + D^{uu}_2 E^1 \tilde{v}^n_{i,j,k} \Big) \nabla_h E^2 U^n_{i,j,k} \Big) \\ \qquad + \nabla_h \cdot \Big(D^{uv}(E^1 u^n_{i,j,k}, E^1 v^n_{i,j,k}) \nabla_h E^2 \tilde{v}^n_{i,j,k} \\ \qquad + \Big(D^{uv}_1 E^1 \tilde{u}^n_{i,j,k} + D^{uv}_2 E^1 \tilde{v}^n_{i,j,k} \Big) \nabla_h E^2 V^n_{i,j,k} \Big) + R^{U,n+1/2}_{i,j,k}, \\ \dfrac{\tilde{v}^{n+1}_{i,j,k} - \tilde{v}^n_{i,j,k}}{\Delta t} = \nabla_h \cdot \Big(D^{vu}(E^1 u^n_{i,j,k}, E^1 v^n_{i,j,k}) \nabla_h E^2 \tilde{u}^n_{i,j,k} \\ \qquad + \Big(D^{vu}_1 E^1 \tilde{u}^n_{i,j,k} + D^{vu}_2 E^1 \tilde{v}^n_{i,j,k} \Big) \nabla_h E^2 U^n_{i,j,k} \Big) \\ \qquad + \nabla_h \cdot \Big(D^{vv}(E^1 u^n_{i,j,k}, E^1 v^n_{i,j,k}) \nabla_h E^2 \tilde{v}^n_{i,j,k} \\ \qquad + \Big(D^{vv}_1 E^1 u^n_{i,j,k} + D^{vv}_2 E^1 v^n_{i,j,k} \Big) \nabla_h E^2 V^n_{i,j,k} \Big) + R^{V,n+1/2}_{i,j,k}. \end{cases} \tag{2.6}$$

Here the coefficients are given by

$$D^{uu}_1 = \partial_u D^{uu}(E^1 \xi^{uu}_{i,j,k}, E^1 \eta^{uu}_{i,j,k}), \; D^{uu}_2 = \partial_v D^{uu}(E^1 \xi^{uu}_{i,j,k}, E^1 \eta^{uu}_{i,j,k}),$$
$$D^{uv}_1 = \partial_u D^{uv}(E^1 \xi^{uv}_{i,j,k}, E^1 \eta^{uv}_{i,j,k}), \; D^{uv}_2 = \partial_v D^{uv}(E^1 \xi^{uv}_{i,j,k}, E^1 \eta^{uv}_{i,j,k}),$$

$$D_1^{uu} = \partial_u D^{uu}(E^1\xi_{i,j,k}^{uu}, E^1\eta_{i,j,k}^{uu}),\ D_2^{uu} = \partial_v D^{uu}(E^1\xi_{i,j,k}^{uu}, E^1\eta_{i,j,k}^{uu}),$$
$$D_1^{uv} = \partial_u D^{uv}(E^1\xi_{i,j,k}^{uv}, E^1\eta_{i,j,k}^{uv}),\ D_2^{uv} = \partial_v D^{uv}(E^1\xi_{i,j,k}^{uv}, E^1\eta_{i,j,k}^{uv}),$$
$$D_1^{vv} = \partial_u D^{vv}(E^1\xi_{i,j,k}^{vv}, E^1\eta_{i,j,k}^{vv}),\ D_2^{vv} = \partial_v D^{vv}(E^1\xi_{i,j,k}^{vv}, E^1\eta_{i,j,k}^{vv}),$$

where $\xi_{i,j,k}^{s_1s_2}$ (for $s_1, s_2 = u$ or v) are numbers between $U_{i,j,k}^n$ and $u_{i,j,k}^n$, and $\eta_{i,j,k}^{s_1s_2}$ (for $s_1, s_2 = u$ or v) are numbers between $V_{i,j,k}^n$ and $v_{i,j,k}^n$, respectively.

An unconditional $\ell^\infty(0, T^*; \ell^2)$ stability estimate for the numerical scheme (2.1) could be derived via its inner product with E^2u^n, E^2v^n, respectively, under certain appropriate assumptions on the diffusion coefficient matrix. On the other hand, such an $\ell^\infty(0, T^*; \ell^2)$ bound for the numerical solution is not sufficient to go through the convergence analysis for the nonlinear equations. A more careful estimate reveals that, an $\ell^\infty(0, T^*; \ell^\infty)$ bound for the numerical solution is needed in the $\ell^\infty(0, T^*; \ell^2) \cap \ell^2(0, T^*; H_h^1)$ error estimate. To conduct a linearized stability analysis, we make the following numerical error assumptions at time steps t^n and t^{n-1}:

$$\|\widetilde{u}^n\|_\infty \le 1,\ \|\widetilde{u}^{n-1}\|_\infty \le 1,\ \|\widetilde{v}^n\|_\infty \le 1,\ \|\widetilde{v}^{n-1}\|_\infty \le 1. \tag{2.7}$$

As a result, it follows from the regularity assumption (A2) that

$$\begin{aligned}
&\|u^n\|_\infty = \|U^n - \widetilde{u}^n\|_\infty \le \|U^n\|_\infty + \|\widetilde{u}^n\|_\infty \le C^* + 1,\\
&\|u^{n-1}\|_\infty = \|U^{n-1} - \widetilde{u}^{n-1}\|_\infty \le \|U^{n-1}\|_\infty + \|\widetilde{u}^{n-1}\|_\infty \le C^* + 1,\\
&\|v^n\|_\infty = \|V^n - \widetilde{v}^n\|_\infty \le \|V^n\|_\infty + \|\widetilde{v}^n\|_\infty \le C^* + 1,\\
&\|v^{n-1}\|_\infty = \|V^{n-1} - \widetilde{v}^{n-1}\|_\infty \le \|V^{n-1}\|_\infty + \|\widetilde{v}^{n-1}\|_\infty \le C^* + 1,
\end{aligned} \tag{2.8}$$

where C^* comes from the regularity of the exact solutions U and V.

Taking a discrete l^2 inner product of the first equation of (2.6) with $E^2\widetilde{u}^n$, we have

$$\begin{aligned}
\langle \frac{\widetilde{u}^{n+1} - \widetilde{u}^n}{\Delta t}, E^2\widetilde{u}^n\rangle &= \langle \nabla_h \cdot \left[D^{uu}(E^1u^n, E^1v^n)\nabla_h E^2\widetilde{u}^n\right], E^2\widetilde{u}^n\rangle\\
&+ \langle \nabla_h \cdot \left[\left(D_1^{uu}E^1\widetilde{u}^n + D_2^{uu}E^1\widetilde{v}^n\right)\nabla_h E^2U^n\right], E^2\widetilde{u}^n\rangle\\
&+ \langle \nabla_h \cdot \left[D^{uv}(E^1u^n, E^1v^n)\nabla_h E^2\widetilde{v}^n\right], E^2\widetilde{u}^n\rangle\\
&+ \langle \nabla_h \cdot \left[\left(D_1^{uv}E^1\widetilde{u}^n + D_2^{uv}E^1\widetilde{v}^n\right)\nabla_h E^2V^n\right], E^2\widetilde{u}^n\rangle + \langle R^{U,n+1/2}, E^2\widetilde{u}^n\rangle.
\end{aligned}$$

The first term could be estimated as follows:

$$\langle \widetilde{u}^{n+1} - \widetilde{u}^n, E^2\widetilde{u}^n\rangle = \langle \widetilde{u}^{n+1} - \widetilde{u}^n, 1\widetilde{u}^{n+1} - 1\widetilde{u}^n + 1(\widetilde{u}^{n+1} - 2\widetilde{u}^n + \widetilde{u}^{n-1})\rangle$$

$$\ge \left(\frac{1}{2}\|\widetilde{u}^{n+1}\|_2^2 + \frac{1}{8}\|\widetilde{u}^{n+1} - \widetilde{u}^n\|_2^2\right) - \left(\frac{1}{2}\|\widetilde{u}^n\|_2^2 + \frac{1}{8}\|\widetilde{u}^n - \widetilde{u}^{n-1}\|_2^2\right),$$

where we have used Cauchy's inequality in the last step. For the terms associated with the nonlinear error terms, an application of the Lemma 2.1 yields

$$\begin{aligned}
&\langle \nabla_h \cdot \left[D^{uu}(E^1u^n, E^1v^n)\nabla_h E^2\widetilde{u}^n\right], E^2\widetilde{u}^n\rangle + \langle \nabla_h \cdot \left[D^{uv}(E^1u^n, E^1v^n)\nabla_h E^2\widetilde{v}^n\right], E^2\widetilde{u}^n\rangle\\
&= -\left(D^{uu}(E^1u^n, E^1v^n)\nabla_h E^2\widetilde{u}^n + D^{uv}(E^1u^n, E^1v^n)\nabla_h E^2\widetilde{v}^n, \nabla_h E^2\widetilde{u}^n\right),
\end{aligned}$$

and

$$\begin{aligned}
&\langle \nabla_h \cdot \left(D_1^{uu}E^1u^n + D_2^{uu}E^1v^n\right)\nabla_h E^2U^n, E^2u^n\rangle\\
&= -\left(D_1^{uu}E^1u^n + D_2^{uu}E^1v^n\right)\nabla_h E^2U^n, \nabla_h E^2u^n\\
&\le C_u\left(\|E^1u^n\|_2\|\nabla_h E^2u^n\|_2 + \|E^1v^n\|_2\|\nabla_h E^2u^n\|_2\right)
\end{aligned}$$

$$\leq \frac{d^u}{8}\|\nabla_h E^2\widetilde{u}^n\|_2^2 + \frac{2C_{uu}^2}{d^u}\|E^1\widetilde{u}^n\|_2^2 + \frac{d^u}{8}\|\nabla_h E^2\widetilde{u}^n\|_2^2 + \frac{2C_{uu}^2}{d^u}\|E^1\widetilde{v}^n\|_2^2,$$

where the constant C_{uu} is related to $\bar{C}$ and $\|U\|_{L^\infty([0,T;W^{1,\infty}])}$, and d^u is the lower bound of the function $D^{uu} - \left|D^{uv} + D^{vu}\right|/2$, cf. the assumption (A3). Also notice that we have used the assumption (2.7) in the first inequality. Similarly, we have

$$\begin{aligned}
&\langle \nabla_h \cdot \left[\left(D_1^{uv} E^1\widetilde{u}^n + D_2^{uv} E^1\widetilde{v}^n\right)\nabla_h E^2 V^n\right], E^2\widetilde{u}^n\rangle \\
&= -\left(\left(D_1^{uv} E^1\widetilde{u}^n + D_2^{uv} E^1\widetilde{v}^n\right)\nabla_h E^2 V^n, \nabla_h E^2\widetilde{u}^n\right) \\
&\leq C_{uv}\left(\|E^1\widetilde{u}^n\|_2\|\nabla_h E^2\widetilde{u}^n\|_2 + \|E^1\widetilde{v}^n\|_2\|\nabla_h E^2\widetilde{u}^n\|_2\right) \\
&\leq \frac{d^u}{8}\|\nabla_h E^2\widetilde{u}^n\|_2^2 + \frac{2C_{uv}^2}{d^u}\|E^1\widetilde{u}^n\|_2^2 + \frac{d^u}{8}\|\nabla_h E^2\widetilde{u}^n\|_2^2 + \frac{2C_{uv}^2}{d^u}\|E^1\widetilde{v}^n\|_2^2,
\end{aligned}$$

where the constant C_{uv} is related to $\bar{C}$ and $\|V\|_{L^\infty([0,T;W^{1,\infty}])}$. Again, we have used the assumption (2.7) in the first inequality. By the truncation error expansion (2.5), we get

$$\langle R^{U,n+1/2}, E^2\widetilde{u}^n\rangle \leq \|E^2\widetilde{u}^n\|_2^2 + \frac{1}{4}\|\Delta t^2 f^{U,n+1/2} + h^2 g^{U,n+1/2}\|_2^2 \leq \|E^2\widetilde{u}^n\|_2^2 + C_u^R\left(\Delta t^4 + h^4\right),$$

where C_u^R is a constant related to $\|f^{U,n+1/2}\|_\infty$ and $\|g^{U,n+1/2}\|_\infty$. Combining all the estimates above, we arrive at

$$\begin{aligned}
&\left(\frac{1}{2}\|\widetilde{u}^{n+1}\|_2^2 + \frac{1}{8}\|\widetilde{u}^{n+1} - \widetilde{u}^n\|_2^2\right) - \left(\frac{1}{2}\|\widetilde{u}^n\|_2^2 + \frac{1}{8}\|\widetilde{u}^n - \widetilde{u}^{n-1}\|_2^2\right) \\
&\leq -\Delta t\left(D^{uu}(E^1u^n, E^1v^n)\nabla_h E^2\widetilde{u}^n + D^{uv}(E^1u^n, E^1v^n)\nabla_h E^2\widetilde{v}^n, \nabla_h E^2\widetilde{u}^n\right) \\
&\quad + \Delta t\frac{d^u}{2}\|\nabla_h E^2\widetilde{u}^n\|_2^2 + 2\Delta t\frac{\left(C_{uu}^2 + C_{uv}^2\right)}{d^u}\left(\|E^1\widetilde{u}^n\|_2^2 + \|E^1\widetilde{v}^n\|_2^2\right) + \Delta t\|E^2\widetilde{u}^n\|_2^2 \\
&\quad + \Delta t C_u^R\left(\Delta t^4 + h^4\right).
\end{aligned} \tag{2.9}$$

Similarly, it follows from the second equation of (2.6) that

$$\begin{aligned}
&\left(\frac{1}{2}\|\widetilde{v}^{n+1}\|_2^2 + \frac{1}{8}\|\widetilde{v}^{n+1} - \widetilde{v}^n\|_2^2\right) - \left(\frac{1}{2}\|\widetilde{v}^n\|_2^2 + \frac{1}{8}\|\widetilde{v}^n - \widetilde{v}^{n-1}\|_2^2\right) \\
&\leq -\Delta t\left(D^{vu}(E^1u^n, E^1v^n)\nabla_h E^2\widetilde{u}^n + D^{vv}(E^1u^n, E^1v^n)\nabla_h E^2\widetilde{v}^n, \nabla_h E^2\widetilde{v}^n\right) \\
&\quad + \Delta t\frac{d^v}{2}\|\nabla_h E^2\widetilde{v}^n\|_2^2 + 2\Delta t\frac{\left(C_{vu}^2 + C_{vv}^2\right)}{d^v}\left(\|E^1\widetilde{u}^n\|_2^2 + \|E^1\widetilde{v}^n\|_2^2\right) + \Delta t\|E^2\widetilde{v}^n\|_2^2
\end{aligned} \tag{2.10}$$

$$\begin{aligned}
&\left(\frac{1}{2}\|\widetilde{u}^{n+1}\|_2^2 + \frac{1}{8}\|\widetilde{u}^{n+1} - \widetilde{u}^n\|_2^2 + \frac{1}{2}\|\widetilde{v}^{n+1}\|_2^2 + \frac{1}{8}\|\widetilde{v}^{n+1} - \widetilde{v}^n\|_2^2\right) \\
&\quad - \left(\frac{1}{2}\|\widetilde{u}^n\|_2^2 + \frac{1}{8}\|\widetilde{u}^n - \widetilde{u}^{n-1}\|_2^2 + \frac{1}{2}\|\widetilde{v}^n\|_2^2 + \frac{1}{8}\|\widetilde{v}^n - \widetilde{v}^{n-1}\|_2^2\right) \\
&\leq \frac{\Delta t}{2}\left(d^u\|\nabla_h E^2 u^n\|_2^2 + d^v\|\nabla_h E^2 v^n\|_2^2\right) \\
&\quad - \Delta t\ D^{uu}(E^1\underset{\sim}{u}^n, E^1v^n)\nabla_h E^2\underset{\sim}{u}^n, \nabla_h E^2 u^n\ - \Delta t\ D^{vv}(E^1u^n, E^1v^n)\nabla_h E^2 v^n, \nabla_h E^2 v^n \\
&\quad + \Delta t\left(D^{uv}(E^1u^n, E^1v^n\ \ ^{vu}(E^1u^n, \widetilde{E}^1v^n)\ _h E^2v^n\ _h E^2u^n\ \ \Delta t\ \widetilde{E}^2u^n\ \tfrac{2}{2}\widetilde{\ }\right)^2 v^n\ \tfrac{2}{2}
\end{aligned}$$

$$
\begin{aligned}
&+2\Delta t\left(\frac{C_{uu}^2+C_{uv}^2}{d^u}+\frac{C_{vu}^2+C_{vv}^2}{d^v}\right)\left(\|E^1\widetilde{u}^n\|_2^2+\|E^1\widetilde{v}^n\|_2^2\right)+\Delta t\left(C_u^R+C_v^R\right)\left(\Delta t^4+h^4\right)\\
&\le-\frac{\Delta t}{2}\left(d^u\|\nabla_h E^2\widetilde{u}^n\|_2^2+d^v\|\nabla_h E^2\widetilde{v}^n\|_2^2\right)+\Delta t\left(\|E^2\widetilde{u}^n\|_2^2+\|E^2\widetilde{v}^n\|_2^2\right)\\
&\quad+2\Delta t\left(\frac{C_{uu}^2+C_{uv}^2}{d^u}+\frac{C_{vu}^2+C_{vv}^2}{d^v}\right)\left(\|E^1\widetilde{u}^n\|_2^2+\|E^1\widetilde{v}^n\|_2^2\right)+\Delta t\left(C_u^R+C_v^R\right)\left(\Delta t^4+h^4\right)\\
&\le-\frac{3}{16}\Delta t\left(d^u\|\nabla_h\widetilde{u}^{n+1}\|_2^2+d^v\|\nabla_h\widetilde{v}^{n+1}\|_2^2\right)+\frac{1}{16}\Delta t\left(d^u\|\nabla_h\widetilde{u}^{n-1}\|_2^2+d^v\|\nabla_h\widetilde{v}^{n-1}\|_2^2\right)\\
&\quad+\Delta t\widetilde{C}_u\left(\|\widetilde{u}^{n+1}\|_2^2+\|\widetilde{u}^n\|_2^2+\|\widetilde{u}^{n-1}\|_2^2\right)+\Delta t\widetilde{C}_v\left(\|\widetilde{v}^{n+1}\|_2^2+\|\widetilde{v}^n\|_2^2+\|\widetilde{v}^{n-1}\|_2^2\right)\\
&\quad+\Delta t\left(C_u^R+C_v^R\right)\left(\Delta t^4+h^4\right),
\end{aligned}
$$

where the constants $\widetilde{C}_u=\max\{\frac{3}{4},\frac{6C_{uu}^2+6C_{uv}^2}{d^u},\frac{1}{4}+\frac{2C_{uu}^2+2C_{uv}^2}{d^u}\}$ and $\widetilde{C}_v=\max\{\frac{3}{4},\frac{6C_{vu}^2+6C_{vv}^2}{d^v},\frac{1}{4}+\frac{2C_{vu}^2+2C_{vv}^2}{d^v}\}$. Here we used the assumption (A3) for diffusion coefficients in the first inequality. A summation in time gives

$$
\begin{aligned}
&\|\widetilde{u}^{n+1}\|_2^2+\frac{1}{4}\Delta td^u\sum_{k=2}^{n+1}\|\nabla_h\widetilde{u}^k\|_2^2+\|\widetilde{v}^{n+1}\|_2^2+\frac{1}{4}\Delta td^v\sum_{k=2}^{n+1}\|\nabla_h\widetilde{v}^k\|_2^2\\
&\le\frac{1}{8}\Delta td^u\|\nabla_h\widetilde{u}^1\|_2^2+\frac{5}{4}\|\widetilde{u}^1\|_2^2+6\Delta t\widetilde{C}_u\sum_{k=1}^{n+1}\|\widetilde{u}^k\|_2^2+\frac{1}{8}\Delta td^v\|\nabla_h\widetilde{v}^1\|_2^2+\frac{5}{4}\|\widetilde{v}^1\|_2^2+6\Delta t\widetilde{C}_v\sum_{k=1}^{n+1}\|\widetilde{v}^k\|_2^2\\
&\quad+2n\Delta t\left(C_u^R+C_v^R\right)\left(\Delta t^4+h^4\right),
\end{aligned}
$$

where the fact that $\widetilde{u}^0\equiv0$ and $\widetilde{v}^0\equiv0$ have been used. From the estimates of the error functions at the first time step, cf. Appendix A, we have

$$
\begin{aligned}
&\|\widetilde{u}^{n+1}\|_2^2+\frac{1}{4}\Delta td^u\sum_{k=2}^{n+1}\|\nabla_h\widetilde{u}^k\|_2^2+\|\widetilde{v}^{n+1}\|_2^2+\frac{1}{4}\Delta td^v\sum_{k=2}^{n+1}\|\nabla_h\widetilde{v}^k\|_2^2\\
&\le6\Delta t\widetilde{C}_u\sum_{k=1}^{n+1}\|\widetilde{u}^k\|_2^2+6\Delta t\widetilde{C}_v\sum_{k=1}^{n+1}\|\widetilde{v}^k\|_2^2+\frac{1}{4}\widetilde{C}^R\left(\Delta t^4+h^4\right),
\end{aligned}
$$

where $\widetilde{C}^R=8T\left(C_u^R+C_v^R\right)+\frac{21}{2}\widetilde{C}_\tau$. By assuming that $\Delta t\le\min\{\frac{\widetilde{C}_u^{-1}}{8},\frac{\widetilde{C}_v^{-1}}{8}\}$, we have

$$
\begin{aligned}
&\|\widetilde{u}^{n+1}\|_2^2+\Delta td^u\sum_{k=2}^{n+1}\|\nabla_h\widetilde{u}^k\|_2^2+\|\widetilde{v}^{n+1}\|_2^2+\Delta td^v\sum_{k=2}^{n+1}\|\nabla_h\widetilde{v}^k\|_2^2\\
&\le24\Delta t\widetilde{C}_u\sum_{k=1}^{n}\|\widetilde{u}^k\|_2^2+24\Delta t\widetilde{C}_v\sum_{k=1}^{n}\|\widetilde{v}^k\|_2^2+\widetilde{C}^R\left(\Delta t^4+h^4\right).
\end{aligned}
$$

An application of the discrete Gronwall inequality implies a numerical convergence in $\ell^\infty(0,T;\ell^2)\cap\ell^2(0,T;H_h^1)$:

where $\widetilde{C}=24\max\{\widetilde{C}_u,\widetilde{C}_v\}$. It follows that

$$
\|u^{n+1}\|_2+\sqrt{d^u}\left(\Delta t\sum_{k=2}^{n+1}\|\nabla_h u^k\|_2^2\right)^{1/2}+\|v^{n+1}\|_2+\sqrt{d^v}\left(\Delta t\sum_{k=2}^{n+1}\|\nabla_h v^k\|_2^2\right)^{1/2}\le C\left(\Delta t^2+h^2\right),
$$

where $C = 2\sqrt{\quad}$. By Lemma 2.2, we have

$$\|\widetilde{u}^{n+1}\|_\infty + \|\widetilde{v}^{n+1}\|_\infty \le \frac{C^I\left(\|\widetilde{u}^{n+1}\|_2 + \|\widetilde{v}^{n+1}\|_2\right)}{h^{\frac{3}{2}}} \le \frac{C^I C\left(\Delta t^2 + h^2\right)}{h^{\frac{3}{2}}}.$$

By assuming $\Delta t \le C_1 h$ with C_1 being a positive constant, we have the a-priori assumption (2.7) valid at time step t^{n+1}, i.e.,

$$\|\widetilde{u}^{n+1}\|_\infty + \|\widetilde{v}^{n+1}\|_\infty \le C^I C\left(C_1^2 + 1\right)\sqrt{h} \le 1$$

for $h \le C_h$, with the constant $C_h = \left[C^I C\left(C_1^2+1\right)\right]^{-2}$. The restriction on time step can be summarized as $\Delta t < C_r h$ with $C_r = \min\{C_1, \frac{\widetilde{C}_u^{-1}}{8h}, \frac{\widetilde{C}_v^{-1}}{8h}\}$. Therefore, an induction for the assumption (2.7) can be applied. This completes the proof of Theorem 2.1. □

Remark 2.2. An ℓ^∞ bound for the numerical solution is needed in the $\ell^\infty(0,T;\ell^2)\cap\ell^2(0,T;H_h^1)$ error estimate. Meanwhile, such an ℓ^∞ bound is not directly available for the numerical solution. To overcome such an essential difficulty, we make an a-priori assumption (2.7) for the numerical solution at the previous time steps, and recover such an a-priori assumption via the convergence estimate at the next time step.

Remark 2.3. In the numerical scheme (2.1), a modified version of Adams–Moulton interpolation formula, with coefficients $(3/4, 0, 1/4)$ at t^{n+1}, t^n, t^{n-1}, respectively, is applied to the diffusion term. In comparison with the standard Crank–Nicolson approximation, an extra weight has been placed on the implicit time level. This treatment leads to a much improved stability property than the Crank–Nicolson one. In our numerical analysis, the extra weight on implicit time level plays a key role in the $\ell^2(0,T;H_h^1)$ error estimate. In comparison, if the standard Crank–Nicolson scheme is used, a theoretical justification of the analysis will fail to control the terms arising from the linearization process.

Such an improved stability property for the modified $(3/4, 0, 1/4)$ Adams–Moulton interpolation formula has been reported for the Cahn–Hilliard and other related gradient flows; see the related works [13,17,18,24], etc.

3. Numerical tests and applications

3.1. Convergence test

To test the convergence, we apply the numerical scheme to solve the diffusion equations

$$\begin{cases} u_t = \nabla\cdot\left[D^{uu}(u,v)\nabla u + D^{uv}(u,v)\nabla v\right] + f^u, \\ v_t = \nabla\cdot\left[D^{vu}(u,v)\nabla u + D^{vv}(u,v)\nabla v\right] + f^v, \end{cases}$$

with Neumann boundary conditions (1.4). The concentration-dependent diffusion coefficients are given by

$$D^{uu}(u,v) = D^{vv}(u,v) = u^2 + v^2 + 1 \quad \text{and} \quad D^{uv}(u,v) = D^{vu}(u,v) = u^2 + v^2.$$

Initial conditions and source terms f^u and f^v are computed with known exact solutions

$$\begin{cases} u = e^{-t/2}\cos\left(\frac{2\pi}{L_x}x - \pi\right)\cos\left(\frac{2\pi}{L_y}y - \pi\right)\cos\left(\frac{2\pi}{L_z}z - \pi\right), \\ v = e^{-t/2}\cos\left(\frac{4\pi}{L_x}x - 2\pi\right)\cos\left(\frac{2\pi}{L_y}y - \pi\right)\cos\left(\frac{2\pi}{L_z}z - \pi\right). \end{cases}$$

Note that the diffusion coefficients satisfy the assumptions listed in (A1). The numerical solutions are compared with exact solutions in the norms of l^2 and l^∞. We take $\Delta t = h/10$ and simulate the problem up to time $T = 0.5$. The linear system resulting from the discretization is solved by the algebraic multigrid (AMG) method. Table 1 displays errors and computational orders for various spatial and temporal step sizes. It is clearly demonstrated that numerical errors decrease as the mesh refines, and that the numerical scheme is convergent with a second-order accuracy in both l^2 and l^∞ norms.

Table 1

Convergence results of the proposed scheme at $T = 0.5$, using $\Delta t = \frac{h}{10}$.

Grid size	$20 \times 20 \times 20$	$40 \times 40 \times 40$	$80 \times 80 \times 80$	$160 \times 160 \times 160$
l^∞-Error	1.82E-2	4.42E-3	1.10E-3	2.84E-4
Order (l^∞)	–	2.04	2.01	1.95
l^2-Error	1.99E-2	4.54E-3	1.09E-3	2.68E-4
Order (l^2)	–	2.13	2.06	2.02

Table 2
Convergence results of the scheme with diffusion terms discretized by the Crank–Nicolson method at $T = 0.5$, using $\Delta t = \frac{h}{10}$.

Grid Size	$20 \times 20 \times 20$	$40 \times 40 \times 40$	$80 \times 80 \times 80$	$160 \times 160 \times 160$
l^∞-Error	4.60E-2	4.43E-3	1.09E-3	2.84E-4
Order (l^∞)	–	3.38	2.02	1.94
l^2-Error	2.03E-2	4.55E-3	1.09E-3	2.68E-4
Order (l^2)	–	2.16	2.06	2.02

here numerically compare the accuracy of the proposed scheme and the scheme with diffusion terms discretized by the standard Crank–Nicolson method. We choose time step sizes $\Delta t = h/10$, which is stable for both schemes. Comparing the errors and convergence orders listed in Tables 1 and 2, one finds that our scheme is more accurate with a coarse computational mesh, but the accuracy, as well as the convergence order, becomes indistinguishable for both schemes, as the mesh refines. The results demonstrate that, apart from better time-stepping stability, the treatment with a modified version of the Adams–Moulton interpolation formula is as accurate as the standard Crank–Nicolson method.

3.2. Applications

The diffusion equations of aluminum in pure iron was proposed in the work [16]; however, constant diffusion coefficients over entire concentration ranges do not apply well to the Al–Fe system [25,33]. To improve, diffusion equations with concentration-dependent diffusion coefficients were proposed to analyze the kinetics of aluminization process [32]. Nevertheless, there are still some discrepancies between the calculated concentration and the experimental data at the Al-rich intermetallic layer, because a third element (Cr) is not explicitly considered in the equations [49]. In the following sections, we apply the proposed numerical scheme to study the phase formation and evolution of chemical compositions in the annealing reaction of a ternary system.

We simulate a high-temperature annealing of alternatively stacked metal layers that consist of Al and stainless steel (SS) foils. We focus on the concentration of elements Al and Ni, and treat other elements in the stainless steel, such as Fe and Cr, as the diffusion background. We take μm and *hour* as the characteristic length scale and time scale, respectively. We rescale all the concentrations to a characteristic concentration value corresponding to one unit atom percent (at.%) of Fe in the system [49]. Given the symmetry of laminate structures, we choose a computational domain $[-150, 150] \times [-40.5, 40.5] \times [-40.5, 40.5]$ (in µm), in which the left half represents the SS region and the right half represents the Al region. We assume an ideal initial condition that the concentration of Al is 100 at.% in the Al layer and is 0 at.% in the stainless steel layer, and the concentration of Ni is 0 at.% in the Al layer and is 30 at.% in the stainless steel layer. There are sharp jumps of the concentrations across the interface $x = 0$, cf. the initial concentration profile in Fig. 2. The concentration-dependent diffusion coefficients are extracted from experimental results reported in the literature [25]. Interpolation and extrapolation schemes are used to compute the diffusion coefficients that are not directly available.

3.2.1. Evolution of microstructure

In this case, we focus on the evolution of the microstructure of intermetallic layers during an annealing process. Fig. 2 shows the concentrations of Al and Ni at time $T = 0, 1, 2, 3, 4, 5$, and 6 hours, reproducing the formation of the Al-rich layer and Ni-rich layer. Initially, the domains $x < 0$ and $x > 0$ represent the SS layer and Al foil, respectively. As time evolves, the concentrations of Al and Ni develop sharp jumps, and two intermetallic layers, i.e., the inward growth and outward growth layers, begin to form on each side of the SS/intermetallic interface. The inward growth layer presents on the right side of the SS/intermetallic interface with a faster growing speed, while the outward growth layer forms on the left side of the interface and grows into the SS layer a bit slower. This indicates that the diffusion of heavier elements (Fe and Ni) from the SS layer toward the Al side contributes more to the growth of the intermetallic layers. Such a formation pattern agrees with experimental studies reported before [47,49].

The intermetallic layers formed during the annealing can be separated into two parts, based on the percentage of chemical composition of Al in the concentration profiles shown in Fig. 2. One part that contains Al from 100 at.% to 60 at.% is called an Al-rich layer. There are two stages in such an Al-rich layer. The first stage, from 100 at.% Al to 80 at.% Al, corre-

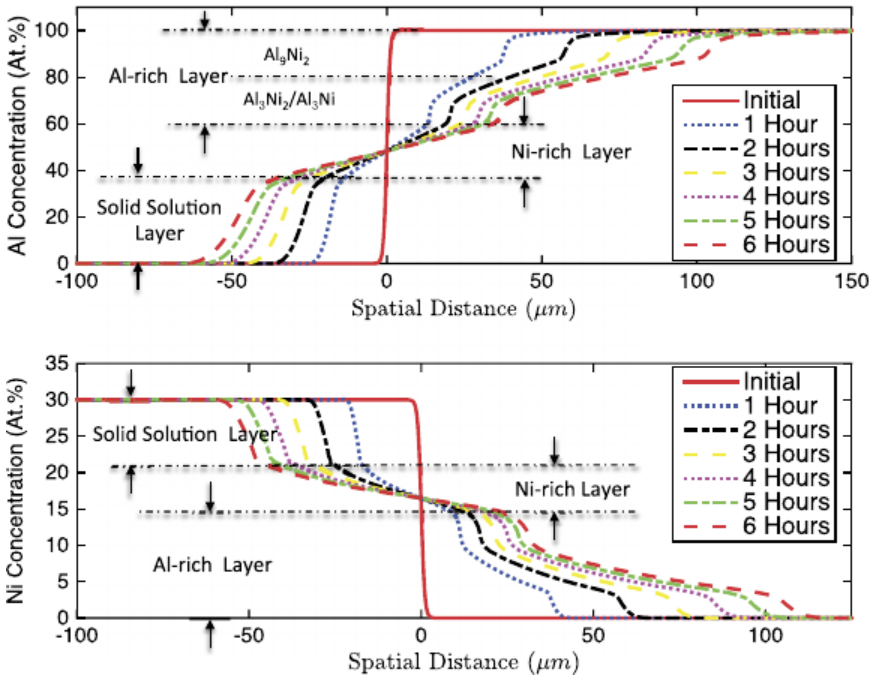

Fig. 2. Al and Ni concentration profiles at time $T = 0, 1, 2, 3, 4, 5, 6$ hours.

the same crystal structure as the Al_9Ni_2, would form when iron participates the Al–Ni intermetallic formation. The other stage in the Al-rich layer, from 80 at.% to 60 at.%, corresponds to the Al_3Ni and Al_3Ni_2 phases in the Al–Ni phase diagram. The presence of iron in the system causes the thermodynamic stability of Al_3Ni and Al_3Ni_2 phases close to each other. It is reasonable to believe that both the Al_3Ni and Al_3Ni_2 phases co-exist in this region, as the concentrations of Al and Ni in this region are between the stoichiometry of these two phases.

In the Ni-rich layer, the concentration of Al, from 40 at.% to 60 at.%, corresponds to the composition of a NiAl phase, which is consistent with the formation of a B2 phase layer [47,49]. From the plots shown in Fig. 2, we observe that Fe also presents in such a B2 phase layer. Previous studies have suggested that, when Fe atoms participate in the formation of the NiAl phase, they partially substitute the central Al atoms in the lattice and keep the B2 structure more stable. Furthermore, both the concentration profiles of Ni and Al predict a solid solution layer with gradually decreasing (increasing) concentrations of Al (Ni) from the B2 phase layer to the stainless steel layer.

Although our numerical simulations can qualitatively reproduce the formation of Al-rich and Ni-rich layers, the calculated concentration profiles of Al and Ni still exhibit some discrepancies from real concentration evolution in an Al–Fe–Ni system, especially in the region where more than one equilibrium compound phases exist. As described above, we know that, in the Al-rich layer, the atom ratio of Al to Ni is between Al_3Ni and Al_3Ni_2 phases; however, we only can conclude that both phases may coexist in the layer. While the real volume percentage of the Al_3Ni and Al_3Ni_2 phases formed in the layer needs to be calculated based on the stability of thermodynamics of the phases in the same experimental conditions. Despite such quantitative discrepancies, the present calculation is still useful for estimating the evolution of microstructure during high-temperature annealing process.

3.2.2. Growth kinetics

As depicted in Fig. 2, an Al-rich layer and Ni-rich layer form during the annealing process. The growth of intermetallic layers are mainly driven by the diffusion of heavy elements, such as Fe and Ni, to the Al layer. To further characterize the growth kinetics of each layer, we study the change of the width of each layer with respect to time evolution. It is well known that, at a given temperature, there is an empirical relationship between the width of a diffusion layer and diffusion time:

$$\Delta x = kt^n, \qquad \text{i.e.,} \quad \ln\Delta x = n\ln t + \ln k,$$

where Δx is the width of the reaction layer, k is the rate constant, t is the elapsed diffusion time, and n is the kinetic

exponent.

The width of each layer is determined by end points where the concentration has sharp changes, cf. Fig. 2. The log–log plot of the width of intermetallic layers against annealing time is displayed in Fig. 3 (Left). The discrete data (shown in stars and diamonds) are measured from concentration profiles, and the dash lines are linear fits of the discrete data. The kinetic

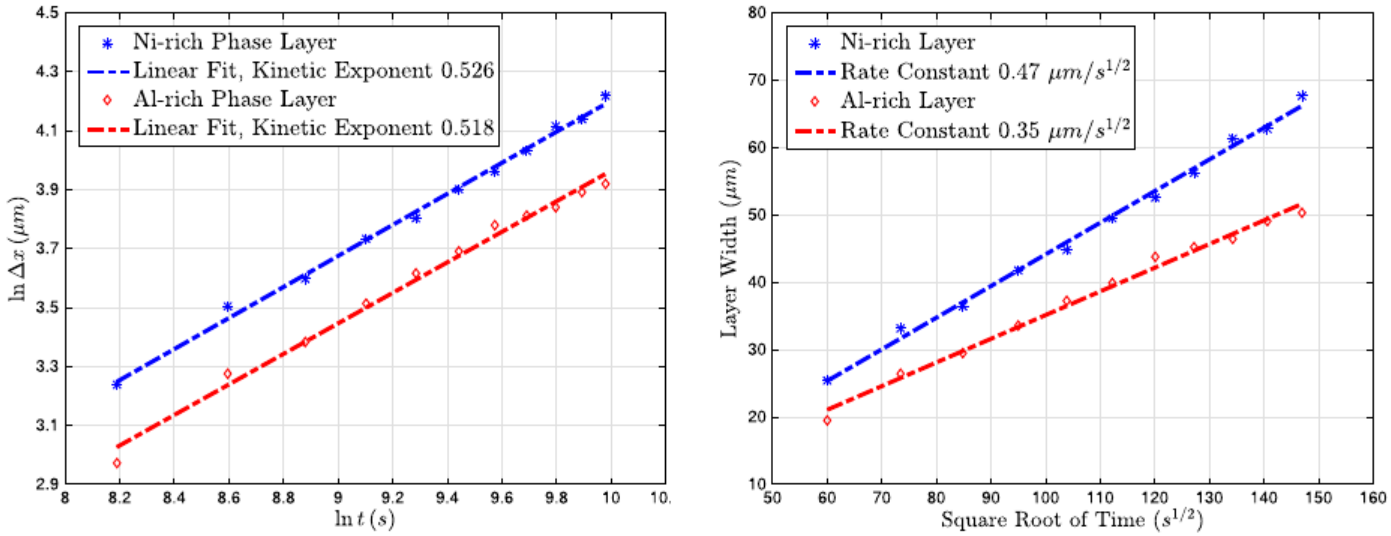

Fig. 3. Left: The log–log plot of the width of intermetallic layers against annealing time. Right: Estimate of rate constant from the dependence of the width of intermetallic layers on annealing time.

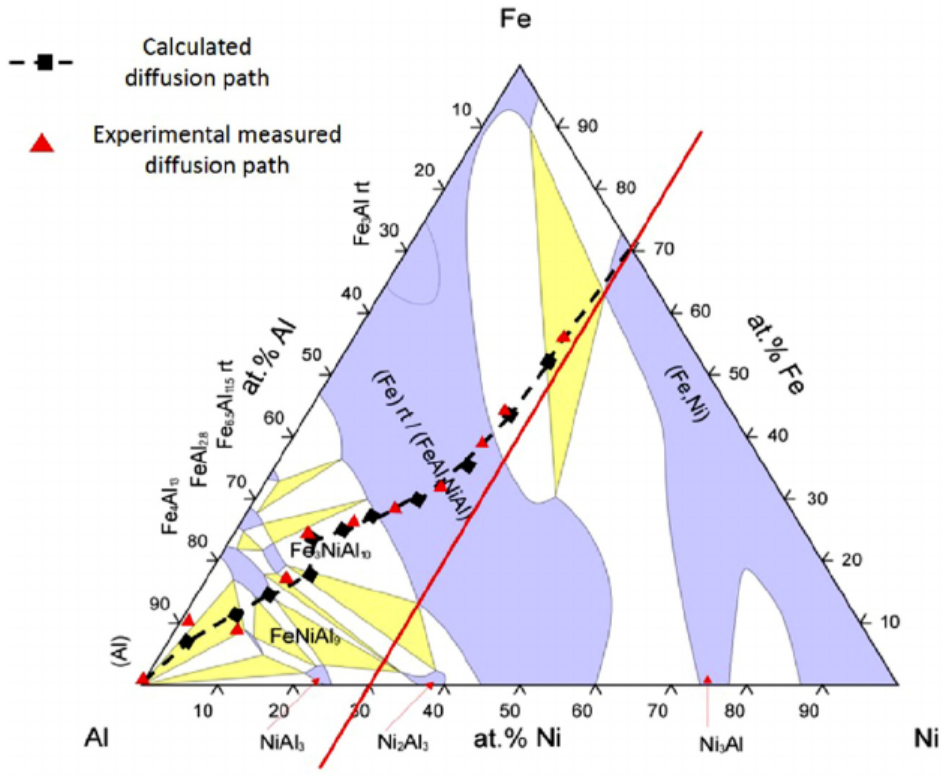

Fig. 4. The ternary phase diagram for the Al–Fe–Ni system and diffusion paths. The diffusion path measured from experiments is presented for comparison.

0.47 μm/s , and that of Ni-rich layer is about 0.35 μm/s . The results are in the same magnitude as the rate constants reported in previous studies on intermetallic annealing reactions [16,27,49].

3.2.3. Ternary phase diagram

To reveal the distribution of concentrations of different elements in a ternary system, it is efficient and helpful to present a diffusion path of different chemical compositions across an intermetallic layer during the annealing process. As displayed in Fig. 4, we sketch a diffusion path in a ternary phase diagram based on our numerical results. For comparison, we also show a measured diffusion path from experimental data [46]. Two diffusion paths both connect two endpoints, corresponding to the Al layer and the SS layer. In the low-Al region, the numerically calculated diffusion path agrees perfectly with

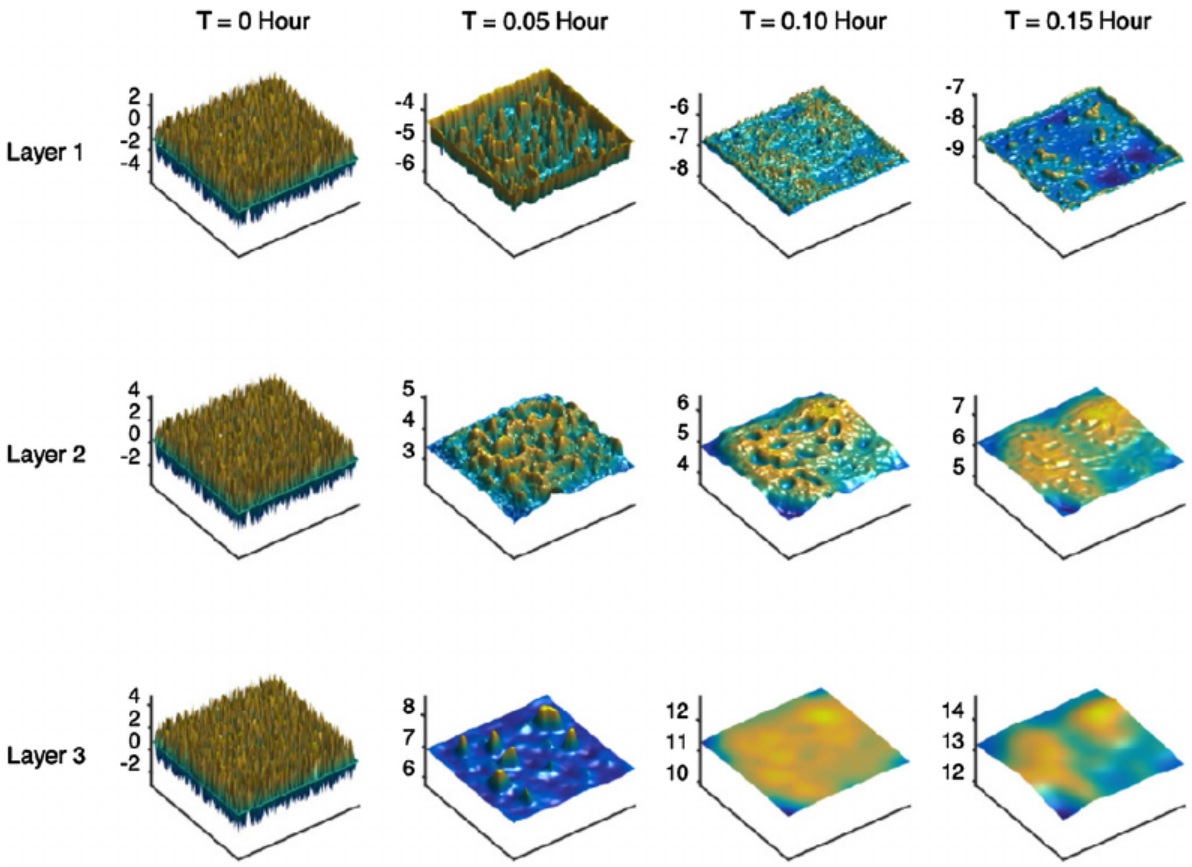

Fig. 5. Evolution of the morphology of interfaces in initial stages of the diffusion.

cal calculations. Overall, our numerical results demonstrate that numerical simulations can effectively capture the diffusion path in the formation process of intermetallic layers in a ternary system.

3.2.4. Layer interface morphology

In real applications, the initial interface between the Al layer and SS layer usually has noises of a small magnitude, rather than a perfect plane. It has been reported that the growth of intermetallic layer begins with nodules initially formed at the interface and proceeds to grow into a continuous layer [47,49]. The noisy interface plays a crucial role in the generation of the nodules. In this case, we study the effect of a noisy interface on the evolution of the interface morphology in the initial stage. In our 3D simulations, we cover the computational domain with a grid size of $400 \times 108 \times 108$, and randomly perturb the initial interface with an amplitude of 2 μm.

We identify three layer interfaces that are between each two of the SS layer, Ni-rich layer, Al-rich layer, and Al layer, by locating the positions where the concentrations of Al have sharp changes. Such three layers are labeled as “Layer 1”, “Layer 2”, and “Layer 3”, in the following contents. Fig. 5 shows the evolution of the morphology of three interfaces in initial stages. Since the initial interface is randomly perturbed, we can see noisy interfaces in the first column of the figure. Later,

the noisy interfaces develop small islands due to the diffusion with concentration-dependent diffusion coefficients. As mentioned above, these islands are reminiscent of intermetallic nodules observed in the experiments [47,49]. As time evolves, the islands are gradually smoothed to flat surfaces by the diffusion. We observe that the Layer 3 is smoothed much faster than the Layer 1 because of larger diffusion coefficients in the environment of high Al concentrations. All of these computational results qualitatively reproduce the morphology of layer interfaces in the formation of the metal–intermetallic-laminate composites.

4. Conclusions

Metal–intermetallic-laminate (MIL) composites are fabricated to improve physical and mechanical performances of metal materials by high-temperature annealing reactions. A cross-diffusion system with concentration-dependent diffusion coefficients have been proposed to describe such as annealing reactions in a ternary system. We have proposed a second-order accurate numerical scheme, both in time and space discretization, for the cross-diffusion system. We have performed a detailed numerical analysis to confirm its stability and second-order accuracy. The accuracy has also been further verified by

experiments. The growth kinetics of such two layers have been systematically characterized by finding the rate constant and kinetic exponent of the diffusion reaction. Further analysis on the diffusion paths, displayed in a ternary phase diagram, has shown that the simulations are in a reasonable agreement with experimental data. In addition, we have investigated the evolution of interface morphology of the two layers, by starting from a randomly perturbed initial interface between the Al layer and stainless steel layer. Overall, comparison of our simulation results with the experimental data has demonstrated the robustness and effectiveness of our proposed numerical scheme in predicting the annealing process of a ternary system.

We now discuss several issues and possible further improvements of our approach. In the numerical simulation of the annealing process, the diffusion coefficients, as functions of two concentrations, should be provided before numerical calculations. However, the diffusion coefficients, measured by experimental techniques, are only available for certain concentrations of Al and Ni. In our current treatment, we obtain the diffusion coefficients by interpolations, which may affect the accuracy of numerical predictions. It is desirable that experimental studies can provide better resolution of the diffusion coefficients when they have large variations with respect to concentrations.

As solutions to a ternary cross-diffusion system, the concentrations of diffusion metal elements should be nonnegative. Our numerical analysis has shown that our numerical scheme is stable and convergent, but the numerical solutions have not been rigorously proved to respect the property of nonnegativity. One of the difficulties in proving nonnegativity is the matrix of the linear system after discretization, whose eigenvalues are hard to estimate. Furthermore, the cross diffusion terms contribute to matrix entries that are far away from the diagonal, making iterative solvers much less efficient. To address these issues, numerical schemes based on time-splitting methods will be one of our future works. Corresponding numerical analysis on the stability, convergence, and nonnegativity is also needed.

In this work, we have applied our numerical scheme to an Al–Fe–Ni system, and reproduce many details in the annealing process of MIL composites. As a matter of fact, it can be directly applied to any ternary reaction system, such as an Al–Fe–Cr system. With further refinements on diffusion coefficients, our numerical approach is expected to be a reliable, useful tool in the commercial design and production of MIL composites.

Acknowledgements

This work is supported by National Natural Science Foundation of China (NSFC 11601361 and NSFC 21773165), Natural Science Foundation of Jiangsu Province (BK20160302) (S. Zhou), NSFC 51701185 (Y. Wang), NSFC 11271281 (X. Yue), and NSF DMS-1418689 (C. Wang).

Appendix A

A.1. Estimate of the first time step

Given the exact solution $U(x,t)$ and $V(x,t)$ of the problem (1.1) to (1.4), it follows from the Taylor expansion at $(x_i, y_j, z_k, \Delta t)$ that

$$1 \qquad 0$$

$$\begin{cases} \dfrac{U^1_{i,j,k}-U^0_{i,j,k}}{\Delta t} = \nabla_h\cdot\left[D^{uu}(U^0_{i,j,k},V^0_{i,j,k})\nabla_h U^1_{i,j,k}+D^{uv}(U^0_{i,j,k},V^0_{i,j,k})\nabla_h V^1_{i,j,k}\right]+\tau^U_{i,j,k},\\ \dfrac{V^1_{i,j,k}-V^0_{i,j,k}}{\Delta t} = \nabla_h\cdot\left[D^{vu}(U^0_{i,j,k},V^0_{i,j,k})\nabla_h U^1_{i,j,k}+D^{vv}(U^0_{i,j,k},V^0_{i,j,k})\nabla_h V^1_{i,j,k}\right]+\tau^V_{i,j,k}, \end{cases} \tag{A.1}$$

where the truncation errors satisfy

$$\tau^U_{i,j,k}\le C^U_\tau\left(\Delta t+h^2\right)\ \text{ and }\ \tau^V_{i,j,k}\le C^V_\tau\left(\Delta t+h^2\right), \tag{A.2}$$

for $i=1,\dots,N_x-1;\ j=1,\dots,N_y-1;\ k=1,\dots,N_z-1$. Here C^U_τ and C^V_τ are associated with certain high order derivatives of exact solutions U and V. Recall the error functions over the grid points:

$$\tilde{u}^1_{i,j,k}=U^1_{i,j,k}-u^1_{i,j,k}\quad\text{and}\quad\tilde{v}^1_{i,j,k}=V^1_{i,j,k}-v^1_{i,j,k}.$$

We assume that the initial time step $u^0_{i,j,k}$ and $v^0_{i,j,k}$ are exact, i.e., $\tilde{u}^0_{i,j,k}\equiv 0$ and $\tilde{v}^0_{i,j,k}\equiv 0$. Subtracting (2.2) from (A.1), we have

$$\begin{cases} \dfrac{\tilde{u}^1_{i,j,k}}{\Delta t} = \nabla_h\cdot\left[D^{uu}(U^0,\dots,V^0,\dots)\nabla_h\tilde{u}^1,\dots+D^{uv}(U^0,\dots,V^0,\dots)\nabla_h\tilde{v}^1,\dots\right]+\tau^U,\dots \end{cases}$$

Taking a discrete l^2 inner product with (A.3) by $\tilde{u}^n$ and $\tilde{v}^n$, respectively, we obtain

$$\begin{cases} \|\tilde{u}^1\|_2^2 = -\Delta t\left(D^{uu}(U^0,V^0)\nabla_h\tilde{u}^1,\nabla_h\tilde{u}^1\right)-\Delta t\left(D^{uv}(U^0,V^0)\nabla_h\tilde{v}^1,\nabla_h\tilde{u}^1\right)+\Delta t\langle\tau^U,\tilde{u}^1\rangle,\\ \|\tilde{v}^1\|_2^2 = -\Delta t\left(D^{vu}(U^0,V^0)\nabla_h\tilde{u}^1,\nabla_h\tilde{v}^1\right)-\Delta t\left(D^{vv}(U^0,V^0)\nabla_h\tilde{v}^1,\nabla_h\tilde{v}^1\right)+\Delta t\langle\tau^V,\tilde{v}^1\rangle, \end{cases} \tag{A.4}$$

where τ^U and τ^V are vectors with components $\tau^U_{i,j,k}$ and $\tau^V_{i,j,k}$, respectively. Notice that we have used Lemma 2.1 in the equations (A.4). Without causing any confusion, we omit U^0 and V^0 in the arguments of D^{uu}, D^{uv}, D^{vu}, and D^{vv}. Adding these two equations together, we have

$$\begin{aligned} &\|\tilde{u}^1\|_2^2+\|\tilde{v}^1\|_2^2\\ &=-\Delta t\left[\left(D^{uu}\nabla_h\tilde{u}^1,\nabla_h\tilde{u}^1\right)+\left(D^{vv}\nabla_h\tilde{v}^1,\nabla_h\tilde{v}^1\right)+\left(\left(D^{uv}+D^{vu}\right)\nabla_h\tilde{v}^1,\nabla_h\tilde{u}^1\right)\right]\\ &\quad+\Delta t\langle\tau^U,\tilde{u}^1\rangle+\Delta t\langle\tau^V,\tilde{v}^1\rangle\\ &\le-\Delta t\left[\left(\left(D^{uu}-\left|\frac{D^{uv}+D^{vu}}{2}\right|\right)\nabla_h\tilde{u}^1,\nabla_h\tilde{u}^1\right)+\left(\left(D^{vv}-\left|\frac{D^{uv}+D^{vu}}{2}\right|\right)\nabla_h\tilde{v}^1,\nabla_h\tilde{v}^1\right)\right]\\ &\quad+\frac{\|\tilde{u}^1\|_2^2}{2}+\frac{\|\tilde{v}^1\|_2^2}{2}+\tilde{C}_\tau(\Delta t^4+h^4), \end{aligned}$$

where $\tilde{C}_\tau$ are constants related to C^U_τ and C^V_τ. In the last inequality, we have made a trivial assumption that the time step size $\Delta t<1$. By the assumption on the diffusion coefficients, we have

$$\frac{\|\tilde{u}^1\|_2^2}{2}+\frac{\|\tilde{v}^1\|_2^2}{2}+\Delta t d^u\|\nabla_h\tilde{u}^1\|_2^2+\Delta t d^v\|\nabla_h\tilde{v}^1\|_2^2\le\tilde{C}_\tau(\Delta t^4+h^4).$$

Therefore, the following estimates have been derived:

$$\begin{aligned} &\|u^1\|_2^2+\|v^1\|_2^2\le 2\tilde{C}_\tau(\Delta t^4+h^4),\\ &\Delta t d^u\|\nabla_h u^1\|_2^2+\Delta t d^v\|\nabla_h v^1\|_2^2\le C_\tau(\Delta t^4+h^4). \end{aligned}$$

~ ~ ~ ~

References

[1] R. Adharapurapu, K. Vecchio, A. Rohatgi, F. Jiang, Fracture of Ti–Al $_3$Ti metallic–intermetallic laminate composites: effects of lamination on resistance-curve behavior, Metall. Mater. Trans. A 36 (2005) 3217–3236.
[2] H. Amann, Dynamic theory of quasilinear parabolic equations. I. Abstract evolution equations, Nonlinear Anal. 12 (1988) 895–919.
[3] H. Amann, Dynamic theory of quasilinear parabolic systems. III. Global existence, Math. Z. 202 (1989) 211–250.
[4] H. Amann, Dynamic theory of quasilinear parabolic equations. II. Reaction–diffusion systems, Differ. Integral Equ. 3 (1990) 13–75.
[5] B. Andreianov, M. Bendahmane, R. Ruiz-Baier, Analysis of a finite volume method for a cross-diffusion model in population dynamics, Math. Models Methods Appl. Sci. 21 (2011) 307–344.
[6] J. Barrett, J. Blowey, Finite element approximation of a nonlinear cross-diffusion population model, Numer. Math. 98 (2004) 195–221.
[7] A. Baskaran, Z. Hu, J. Lowengrub, C. Wang, S.M. Wise, P. Zhou, Energy stable and efficient finite-difference nonlinear multigrid schemes for the modified phase field crystal equation, J. Comput. Phys. 250 (2013) 270–292.
[8] A. Baskaran, J. Lowengrub, C. Wang, S. Wise, Convergence analysis of a second order convex splitting scheme for the modified phase field crystal equation, SIAM J. Numer. Anal. 51 (2013) 2851–2873.
[9] M. Burger, M. Francesco, J. Pietschmann, B. Schlake, Nonlinear cross-diffusion with size exclusion, SIAM J. Math. Anal. 42 (2010) 2842–2871.
[10] M. Chapwanya, J. Lubuma, R. Mickens, Positivity-preserving nonstandard finite difference schemes for cross-diffusion equations in biosciences, Comput. Math. Appl. 68 (2014) 1071–1082.
[11] M.B. Chatard, A. Jungel, A finite volume scheme for a Keller–Segel model with additional cross-diffusion, IMA J. Numer. Anal. 34 (2014) 96–122.
[12] L. Chen, A. Jungel, Analysis of a multi-dimensional parabolic population model with strong cross-diffusion, SIAM J. Math. Anal. 36 (2004) 301–322.
[13] W. Chen, W. Feng, Y. Liu, C. Wang, S.M. Wise, A second order energy stable scheme for the Cahn–Hilliard–Hele–Shaw equation, Discrete Contin. Dyn. Syst., Ser. B (2017), http://doi.org/10.3934/dcdsb.2018090.
[14] W. Chen, Y. Liu, C. Wang, S. Wise, Convergence analysis of a fully discrete finite difference scheme for Cahn–Hilliard–Hele–Shaw equation, Math. Comput. 85 (2016) 2231–2257.
[15] W. Chen, C. Wang, S.M. Wise, X. Wang, A positivity-preserving, energy stable numerical scheme for the Cahn–Hilliard equation with logarithmic potential, SIAM J. Numer. Anal. (2018), Submitted and in review.
[16] C. Christoglou, N. Voudouris, G. Angelopoulos, Formation and modeling of aluminide coatings on iron by a fluidised bed CVD process, Surf. Coat. Technol. 155 (2002) 51–58.
[17] A. Diegel, C. Wang, X. Wang, S.M. Wise, Convergence analysis and error estimates for a second order accurate finite element method for the Cahn–Hilliard–Navier–Stokes system, Numer. Math. 137 (2017) 495–534.
[18] A. Diegel, C. Wang, S.M. Wise, Stability and convergence of a second order mixed finite element method for the Cahn–Hilliard equation, IMA J. Numer. Anal. 36 (2016) 1867–1897.

[21] W. Feng, C. Wang, S.M. Wise, Z. Zhang, A second-order energy stable backward differentiation formula method for the epitaxial thin film equation with slope selection, Numer. Methods Partial Differ. Equ. (2018), https://doi.org/10.1002/num.22271.
[22] D. Gilbarg, N.S. Trudinger, Elliptic Partial Differential Equations of Second Order, 2nd edition, Springer-Verlag, 1998.
[23] S. Gottlieb, C. Wang, Stability and convergence analysis of fully discrete Fourier collocation spectral method for 3-D viscous Burgers' equation, J. Sci. Comput. 53 (2012) 102–128.
[24] J. Guo, C. Wang, S.M. Wise, X. Yue, An H^2 convergence of a second-order convex-splitting, finite difference scheme for the three-dimensional Cahn–Hilliard equation, Commun. Math. Sci. 14 (2016) 489–515.
[25] T. Helander, J. Agren, Diffusion in the B2-B.C.C. phase of the Al–Fe–Ni system – application of a phenomenological model, Acta Mater. 47 (1999) 3291–3300.
[26] Z. Hu, J.S. Lowengrub, S.M. Wise, A. Voigt, Phase-field modeling of epitaxial growth: applications to step trains and island dynamics, Physica D 241 (2012) 77–94.
[27] S. Jozwiak, K. Karczewski, Z. Bojar, Kinetics of reactions in FeAl synthesis studied by the DTA technique and JMA model, Intermetallics 18 (2010) 1332–1337.
[28] A. Jungel, The boundedness-by-entropy method for cross-diffusion systems, Nonlinearity 28 (2015) 1963–2001.
[29] A. Jungel, Entropy Methods for Diffusive Partial Differential Equations, 1st edition, Springer International Publishing, 2016.
[30] Y. Li, C. Zhao, Global existence of solutions to a cross-diffusion system in higher dimensional domains, Discrete Contin. Dyn. Syst. 12 (2005) 185–192.
[31] Y. Lou, W. Ni, Y. Wu, On the global existence of a cross-diffusion system, Discrete Contin. Dyn. Syst. 4 (1998) 193–203.
[32] K. Murakami, N. Nishida, K. Osamura, Y. Tomota, Aluminization of high purity iron by powder liquid coating, Acta Mater. 52 (2004) 1271–1281.
[33] K. Murakami, N. Nishida, K. Osamura, Y. Tomota, T. Suzuki, Aluminization of high purity iron and stainless steel by powder liquid coating, Acta Mater. 52 (2004) 2173–2184.
[34] H. Murakawa, A linear scheme to approximate nonlinear cross-diffusion systems, ESAIM: Math. Model. Numer. Anal. 45 (2011) 1141–1161.
[35] H. Murakawa, A linear finite volume method for nonlinear cross-diffusion systems, Numer. Math. 136 (2017) 1–26.
[36] R. Price, F. Jiang, R. Kulin, K. Vecchio, Effects of ductile phase volume fraction on the mechanical properties of Ti–Al $_3$Ti metal–intermetallic laminate (MIL) composites, Mater. Sci. Eng. A 528 (2011) 3134–3146.
[37] Z. Qiao, C. Wang, S.M. Wise, Z. Zhang, Error analysis of an energy stable finite difference scheme for the epitaxial thin film growth model with slope selection with an improved convergence constant, Int. J. Numer. Anal. Model. 14 (2017) 283–305.
[38] A. Rohatgi, D. Harach, K. Vecchio, K. Harvey, Resistance-curve and fracture behavior of Ti–Al $_3$Ti metal–intermetallic laminate (MIL) composites, Acta Mater. 51 (2003) 2933–2957.
[39] R. Ruiz-Baier, C. Tian, Mathematical analysis and numerical simulation of pattern formation under cross-diffusion, Nonlinear Anal., Real World Appl. 14 (2013) 601–612.
[40] R. Samelson, R. Temam, C. Wang, S. Wang, Surface pressure Poisson equation formulation of the primitive equations: numerical schemes, SIAM J. Numer. Anal. 41 (2003) 1163–1194.
[41] J. Shen, C. Wang, X. Wang, S.M. Wise, Second-order convex splitting schemes for gradient flows with Ehrlich–Schwoebel type energy: application to thin film epitaxy, SIAM J. Numer. Anal. 50 (2012) 105–125.
[42] S. Shim, Uniform boundedness and convergence of solutions to cross-diffusion systems, J. Differ. Equ. 185 (2002) 281–305.

[43] C.
[44] C. Wang, J. Liu, Convergence of gauge method for incompressible flow, Math. Comput. 69 (2000) 1385–1407.
Wang, S.M. Wise, An energy stable and convergent finite-difference scheme for the modified phase field crystal equation, SIAM J. Numer. Anal. 49 (2011) 945–969.
[45] Y. Wang, K. Vecchio, Microstructure evolution in a martensitic 430 stainless steel-al metal–intermetallic laminate (MIL) composite, Mater. Sci. Eng. A 643 (2015) 72–85.
[46] Y. Wang, K. Vecchio, Microstructure evolution in Fe-based-aluminide metal–intermetallic laminate (MIL) composites, Mater. Sci. Eng. A 649 (2015) 325–337.
[47] Y. Wang, H. Wang, X. Liu, K. Vecchio, Microstructure evolution in pure Ni and invar-based metal–intermetallic laminate (MIL) composites, Mater. Sci. Eng. A 682 (2017) 454–465.
[48] Y. Wang, X. Zhang, L. Meng, H. Zhu, M. Zhao, N. Jiang, The microstructure and properties evolution of Al–Si/Al–Mn clad sheet during plastic deformation, J. Mater. Res. 28 (2013) 1601–1608.
[49] Y. Wang, S. Zhou, K. Vecchio, Annealing effects on the microstructure and properties of an Fe-based metallic–intermetallic laminate (MIL) composite, Mater. Sci. Eng. A 665 (2016) 47–58.
[50] S.M. Wise, Unconditionally stable finite difference, nonlinear multigrid simulation of the Cahn–Hilliard–Hele–Shaw system of equations, J. Sci. Comput. 44 (2010) 38–68.
[51] S.M. Wise, C. Wang, J. Lowengrub, An energy stable and convergent finite-difference scheme for the phase field crystal equation, SIAM J. Numer. Anal. 47 (2009) 2269–2288.